IEEE Access
Multidisciplinary | Rapid Review | Open Access Journal

Received June 3, 2019, accepted June 23, 2019, date of publication July 1, 2019, date of current version July 22, 2019.

Digital Object Identifier 10.1109/ACCESS.2019.2925917

Automatic Lumen Segmentation in Intravascular Optical Coherence Tomography Using Morphological Features

HUISHUO ZHAO[1,2,3], BIN HE[1,4,5], ZHENYANG DING[1,2,3], KUIYUAN TAO[1,2,3], TIANDUO LAI[1,2,3], HAO KUANG[6], RUI LIU[7], XIAOGUO ZHANG[8], YICHENG ZHENG[1], JUNYI ZHENG[1], AND TIEGEN LIU[1,2,3]

[1]School of Precision Instruments and Opto-Electronics Engineering, Tianjin University, Tianjin 300072, China
[2]Tianjin Optical Fiber Sensing Engineering Center, Institute of Optical Fiber Sensing of Tianjin University, Tianjin 300072, China
[3]Key Laboratory of Opto-electronics Information Technology, Ministry of Education, Tianjin University, Tianjin 300072, China
[4]State Key Laboratory of Low Dimensional Quantum Physics, Department of Physics, Tsinghua University, Beijing 100084, China
[5]Collaborative Innovation Center of Quantum Matter, Beijing 100084, China
[6]Nanjing Forssmann Medical Technology Company, Nanjing 210002, China
[7]Department of Neurology, Jinling Hospital, Medical School of Nanjing University, Nanjing 210002, China
[8]Department of Cardiology, Zhongda Hospital, School of Medicine, Southeast University, Nanjing 210009, China

Corresponding author: Zhenyang Ding (zyding@tju.edu.cn)

This work was supported in part by the National Natural Science Foundation of China (NSFC) under Grant 61505138, Grant 61635008, and Grant 61735011, in part by the Tianjin Science and Technology Support Plan Program Funding under Grant 16JCQNJC01800, in part by the China Postdoctoral Science Foundation under Grant 2015M580199 and Grant 2016T90205, in part by the National Instrumentation Program under Grant 2013YQ030915, in part by the National Key Research and Development Program under Grant 2016YFC0100500, and in part by the Open Foundation of Key Laboratory of Opto-electronic Information Technology of Ministry of Education, Tianjin University, under Grant 2019KFKT004. Huishuo Zhao and Bin He contributed equally to this work.

ABSTRACT Lumen segmentation in intravascular optical coherence tomography (IVOCT) images is a fundamental work for more advanced plaque analysis, stent recognition, fractional flow reserve (FFR) assessment, and so on. However, the catheter, guide-wire, inadequate blood clearance, and other factors will impact on the accuracy of lumen segmentation. We present a simple and effective method for automatic lumen segmentation method in IVOCT based on morphological features. We use image enhancement, median filtering, image binarization, and morphological closing operation to reduce speckle noise, minimize the effect of blood artifacts and fill in small holes inside vascular walls. We extract the orientation and area-size of connected regions as morphological features in images and remove the catheter and guide-wire completely by morphological corrosion operation, small area-size region removal, and orientation morphological feature comparison, and then the contour of the lumen can be discriminated. The evaluation metrics of this method, the Dice index, Hausdorff distance, Jaccard index, and accuracy of 99.32%, 0.06 mm, 99.4%, and 99.66%, respectively, are obtained from comparing with expert annotations on 268 IVOCT images. Compared with the other morphology-based lumen segmentation methods, the presented method can remove the catheter and guide-wire completely, even if the catheter and guide-wire cling to the lumen or the shape of the catheter is irregular. Since only morphological operations are used to complete all processes, the calculation burden is reduced greatly.

INDEX TERMS Optical coherence tomography, intravascular optical coherence tomography, image segmentation, morphological operation, lumen segmentation.

I. INTRODUCTION

Intravascular Optical Coherence Tomography (IVOCT) is a catheter-based examination method which uses near-infrared light to obtain high-resolution imaging of the *in vivo* vascular wall microstructure [1]–[4]. Vascular lumen contour information has great application value in evaluating the degree of stenosis of blood vessels, obtaining the optimal position of stent implantation and evaluating the adherence condition of stents [5]. In addition, fractional flow reserve (FFR) has been

The associate editor coordinating the review of this manuscript and approving it for publication was Huanqiang Zeng.

TABLE 1. Summary of vascular lumen boundary detection methods.

Method classification	Corresponding paper	Characteristic	Shortcomings
Searching minimum energy theory (Dynamic programming, Level sets)	[8-12]	Continuous iteration, high precision, insensitive to noise	Time consuming, large amount of calculation, vulnerable to wire shadows
Clustering (K-means), especially learning method	[13-15]	Having a great relationship with parameters	Needing to use a lot of training data to learn, sensitive to noise, lots of iterations
Fuzzy system method based on global information	[16]	Fast operation speed	Needing manually participate in setting thresholds for each feature quantity, large amount of calculation
Graph-cut methods	[17-18]	Good robustness	Manually labeling at least one former attraction and one background point, complex, time consuming
Morphology method	[19-21]	Easy operation, fast operation speed, insensitive to intensity variation	Needing to choose proper structuring element

considered as the gold standard for functional assessment of intermediate coronary stenosis. IVOCT can derive FFR by high accuracy lumen segmentation for IVOCT images [6]. Therefore, the accurate identification and segmentation of the vascular lumen contour is particularly important in the treatment of coronary artery disease [7].

In recent years, scholars have proposed series of methods for lumen segmentation in IVOCT are shown in TABLE 1, which includes: 1) Searching minimum energy method based on dynamic programming [8]–[10], or level sets [11], [12]. 2) Clustering method based on K-means [13] or learning method [14], [15]. 3) Fuzzy system method based on global information [16]. 4) Graph-cut method [17], [18]. It is noteworthy that morphology based methods are widely used in lumen segmentation, since they have many advantages including: 1) They are insensitive to intensity variation in images due to binarization process, so they have a robustness for noise. 2) Morphological operations have a low calculation burden. Among morphology based lumen segmentation methods, Moraes *et al.* [19], Celi and Berti [20] and Macedo *et al.* [21] present lumen segmentation approach based on morphology methods with a high accuracy. A wavelet transform is used for an adaptive threshold selection in Otsu binarization [20]. However, these methods remove the catheter by setting pixels in the radial range of the catheter to zero. They will be failure if the catheter cling to the lumen or the shape of catheter is irregular. In addition, the guide-wire is characterized and removed by a bright reflection immediately followed by a shadow [21]. Extra recognition process increase calculation burden. No guide-wire removal process is presented [19].

In this paper, we present a simple and effective method for automatic lumen segmentation method in IVOCT based on morphological features. Firstly, we use image enhancement, median filtering, image binarization and morphological closing operation to reduce speckle noise and minimize the effect of blood artifacts. Secondly, to remove the catheter and guide-wire, we extract the area-size of connected regions in images as a morphological feature, we remove the connected regions with small area-size after processing by a morphological corrosion operation. Thirdly, we identify difference between the orientation and area-size as two morphological features of the residual catheter and blood vessel to remove the residual catheter with a large area-size. And then the contour of the lumen can be discriminated. Finally, the missing contour of the lumen caused by the guide-wire's shadow is reconstructed by a bicubic interpolation. The evaluation metrics of this method, Dice index, Hausdorff distance, Jaccard index and Accuracy of 99.32%, 0.06 mm, 99.4%, 99.55% and 99.66%, respectively are obtained from comparing with expert annotations on 268 IVOCT images. Compared with other morphology based lumen segmentation methods, the presented method can remove the catheter and guide-wire completely, even if the catheter and guide-wire cling to the lumen or the shape of catheter is irregular. Since only the morphological operations are used to complete all processes, the calculation burden is reduced greatly.

II. MATERIALS AND METHODS

A. IMAGE DATA

The segmentation process is mainly divided into three parts: pre-processing, contour extraction and coordinate transformation. The algorithm flow chart is shown in Fig. 1. The data set is selected for processing and analyzing from OCT images database of Jinling Hospital (Nanjing China). The raw data is exported from the IVOCT system (C7XR^{TM}, LightLab Imaging/St. Jude Medical, Westford, MA) for post-processing and frame analysis.

B. PRE-PROCESSING

The image pre-processing mainly includes four parts: image contrast enhancement, filter denoising, image binarization

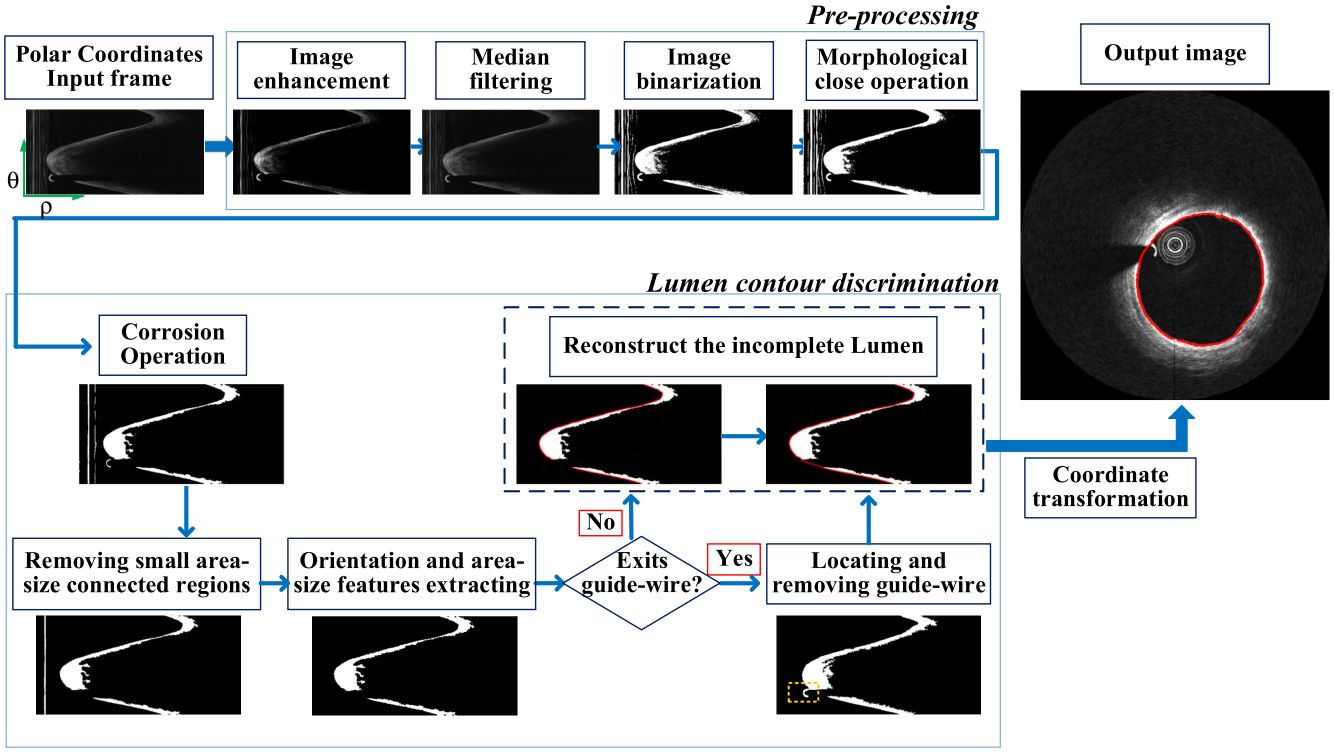

FIGURE 1. Flow chart of lumen segmentation.

and morphological closing operation. In order to avoid losing the original image information, we adjust the gamma coefficient of the image and extend the variation range of the gray value in the original image to a larger gray change interval. Then, the input image under the original 16-bit polar coordinate system is image-enhanced to obtain a clear image. Subsequently, we use a median filter (2×2 median filter) method to remove the speckle noise of the image [22]. Next, to achieve subsequent morphological operation, an image binarization is achieved by the Otsu's automatic thresholding method. Finally, a morphological closing operation is used to fill in small holes inside the vascular wall and minimize the effect of blood artifacts.

C. REMOVAL OF GUIDE-WIRE AND CATHETER

After pre-processing, the catheter and guide-wire portions have a great influence on lumen segmentation [23]. Compared with previous morphology based lumen segmentation methods, we use morphology method to remove the catheter and guide-wire portions, whose calculation burden is reduced greatly due to no extra recognition process for the catheter and guide-wire. In addition, the presented method can remove the catheter and guide-wire completely, even if the catheter and guide-wire cling to the lumen or the shape of catheter is irregular.

For the initial removal of the guide-wire and catheter, a morphological corrosion operation is implemented. In order to choose a reasonable structuring element and avoid a large offset between the original contour of the lumen and the contour processed by a corrosion operation, we attempt different sizes of rectangles and discs as corrosion structuring

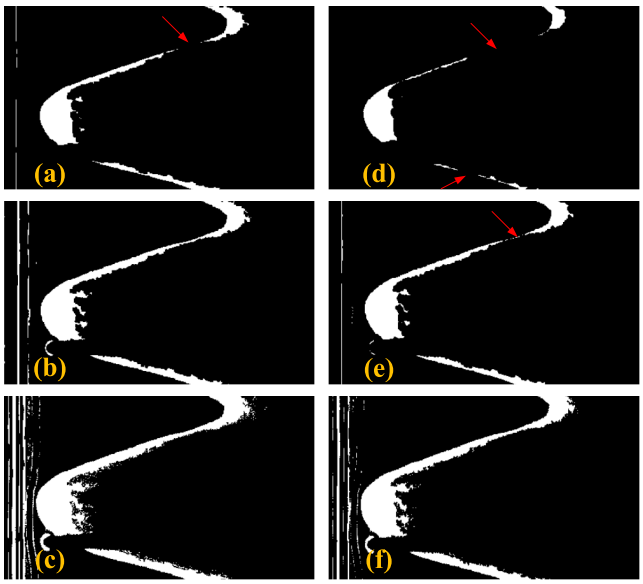

FIGURE 2. Images processed by corrosion operation with different corrosion structuring elements. (a), (b), (c) Rectangular structuring elements with the size of 10 × 10, 5 × 5, 1 × 1, respectively. (d), (e), (f) Disc-shaped structuring elements with a radius of 10, 5 and 1 respectively. The red arrows point to missing and protrusions on the contour of the lumen. The red arrows point to the missing part on contours of the lumen.

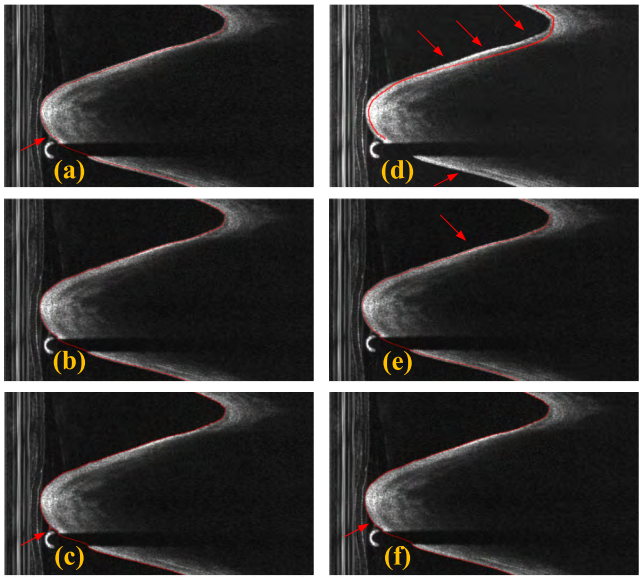

FIGURE 3. Contours of the lumen marked as red lines by different corrosion structuring elements and original image (a), (b), (c) rectangular structural elements with the size of 10 × 10, 5 × 5, 1 × 1, respectively. (d), (e), (f) disc-shaped structuring elements with a radius of 10, 5 and 1 respectively. The red arrows point to the offset between the original contour of the lumen and the contour processed by a corrosion operation.

element, respectively. The images processed by corrosion operation with different corrosion structuring elements are shown in Fig. 2. The contours of the lumen are marked as red lines by different corrosion structuring elements and original image are shown in Fig. 3. From Fig. 3, a larger corrosion structuring elements can cause a more serious missing on contours of the lumen shown in Fig. 2 (a) (d) and (e), which will cause a failure of lumen segmentation shown in Fig. 3 (a) (d) and (e). On the contrary, if the corrosion structuring element is too small, small protrusions on the contours of the lumen caused by blood artifacts and speckle noise are not removed shown in Fig. 3 (c) and (f). In addition, a small corrosion structuring element cannot remove the catheter and guide-wire portions effectively shown in Fig. 2 (c) and (f). Finally, on the basis of the above analysis, we select a rectangular structuring element with a size of 5 × 5 to perform a morphological corrosion operation on images. In addition, from Fig. 3, the catheter cling to the lumen and the shape of catheter is not a straight line, so the catheter cannot be removed easily by setting pixels in the radial range of the catheter to zero.

After morphological corrosion operation, the residual catheter and guide-wire portions still exist in images and there are many connected regions with different area-sizes shown in Fig. 2(b). We need to retain connected regions of blood vessel and remove connected regions of the residual catheter and guide-wire. Here we firstly extract the area-size of connected regions as a morphological feature in images. We attempt to find a threshold of area-size to segment connected regions of blood vessel and others. By statistical analysis of 268 images, we find that the minimum area-sizes (MA) of the connected regions of blood vessel is 0.0133 mm^2 shown Fig. 4(a), we delete the connected regions with area-size of less than 0.0133 mm^2 and list area-size of connected regions in Fig. 4(a). During the statistical analysis of the area-size of connected regions from 268 images, area-sizes of residual catheter's connected regions are also higher than 0.0133 mm^2. We mark area-size of residual catheter's connected regions as the black circle and mark area-size of blood vessel's connected regions. All area-sizes of guide-wire's connected regions are less than 0.0133 mm^2 after processed by morphological corrosion operation.

To remove residual catheter portions completely, using area-size of connected regions as only one morphological feature to process is not enough. From Fig. 2, we find that the geometric shapes of the catheter are mainly linear distribution. The orientation of geometric shape also can be considered as a morphological feature. Therefore, we simultaneously extract orientation and area-size of connected regions as morphological features to remove the residual catheter.

The moment of an image region mainly represents the geometric features, also known as the geometric moment (invariant moment), which can be used to calculate the orientation of connected regions [24], [25]. For grayscale images, if $V(i, j)$ is used to represent the gray value of the image at (i, j) point and its second moment can be used to calculate the orientation of connected regions' shape. The orientation of a connected region can be defined as:

$$\theta = |\frac{arc\tan(b/(a-c))}{2}|, \quad \theta \in [0, 90] \tag{1}$$

where θ is the minimum angle between the x-axis of the image and the orientation of the main axis of the target objects.

$$a = \frac{M_{20}}{M_{00}} - x_c^2, \tag{2}$$

$$b = 2(\frac{M_{11}}{M_{00}} - x_c y_c), \tag{3}$$

$$c = \frac{M_{02}}{M_{00}} - y_c^2, \tag{4}$$

x_c and y_c are the center of gravity coordinates of the image.

$$x_c = \frac{M_{10}}{M_{00}}, \tag{5}$$

$$y_c = \frac{M_{01}}{M_{00}}. \tag{6}$$

Here the moment M_{pq} can be expressed as:

$$M_{pq} = \sum_{i=1}^{I}\sum_{j=1}^{J} i^p j^q V(i, j), \quad p, q = 0, 1, 2, \cdots \tag{7}$$

where M_{00} $(p = q = 0)$ is the zeroth moment. M_{10} $(p = 1, q = 0)$, M_{01} $(p = 0, q = 1)$ are the first moment respectively. M_{20} $(p = 2, q = 0)$, M_{02} $(p = 0, q = 2)$ and M_{11} $(p = 1, q = 1)$ are the second moment respectively. Here, the image to be processed is a binary image, M_{00} is the sum of all the

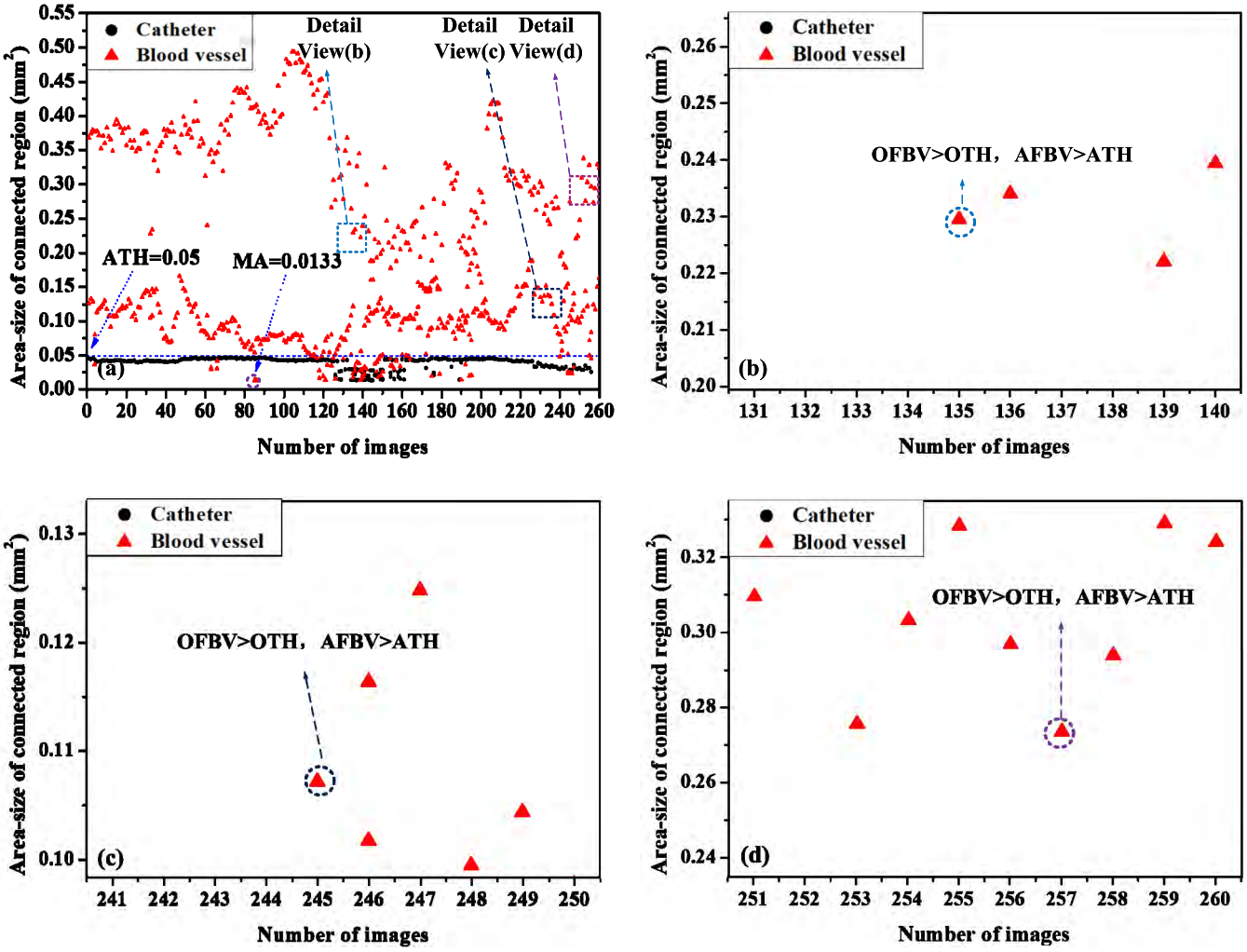

FIGURE 4. (a) Area-size distribution of catheters and blood vessels' connected regions from 268 images. (b), (c) and (d) are detail views of (a)'s dashed box. In (b) (c) and (d)'s dashed circles, area-sizes of connected regions are more than the area-size threshold (0.05 mm^2) marked as a dash line in (a), while orientations of these connected regions are more than the orientation threshold in Fig. 5 (b), (c) and (d). ATH: Area-size threshold. OTH: Orientation threshold. AFBV: Area-size of blood vessel. OFBV: Orientation of blood vessel. The minimum area-size of the connected regions in blood vessel (MA) is 0.0133 mm^2.

value equals to 1 in the connected region. M_{10} is the sum of the x coordinates equal to 1 in the connected region and M_{01} is the sum of the y coordinates equal to 1 in the connected region.

To find an orientation angle threshold of connected regions to segment of blood vessel and the catheter, we calculate the orientation of connected regions with the area-size of more than 0.0133 mm^2 from 268 images based on (1)-(7) and the orientation distribution statistics of the connected regions are drawn as shown in Fig. 5(a). From Fig. 5(a), the orientation angles of straight-shaped catheter portions are mainly concentrated at about 90°, whereas orientation angles of blood vessel portions are relatively dispersed and mainly concentrate at the range of 0-80°. Based on this feature, the catheter and blood vessel portions can be distinguished by selecting a reasonable orientation angle threshold. Here we choose 89.5° as the orientation angle threshold. The orientation angles of all catheter portions. However, from Fig. 5(b) (c) and (d), orientation angles of three blood vessel portions are more than the orientation angle threshold of 89.5°, which will cause segmentation errors. To further eliminate this segment error, we extract area-size of three blood vessel connected regions with segment error, which are shown in Fig. 4 (b), (c) and (d). From Fig. 4(a), the area-size of catheter from 268 images is less than 0.05 mm^2. The area-size of three blood vessel connected regions are much higher than the area-size threshold of 0.05 mm^2 shown in Fig. 4 (b), (c) and (d). The segment condition (SC) for blood vessel and catheter can be expressed as:

$$SC = \begin{cases} A < 0.05mm^2 \parallel O > 89.5° & catheter \\ others & blood\ vessel, \end{cases} \tag{8}$$

where A is area-size and O is orientation angle.

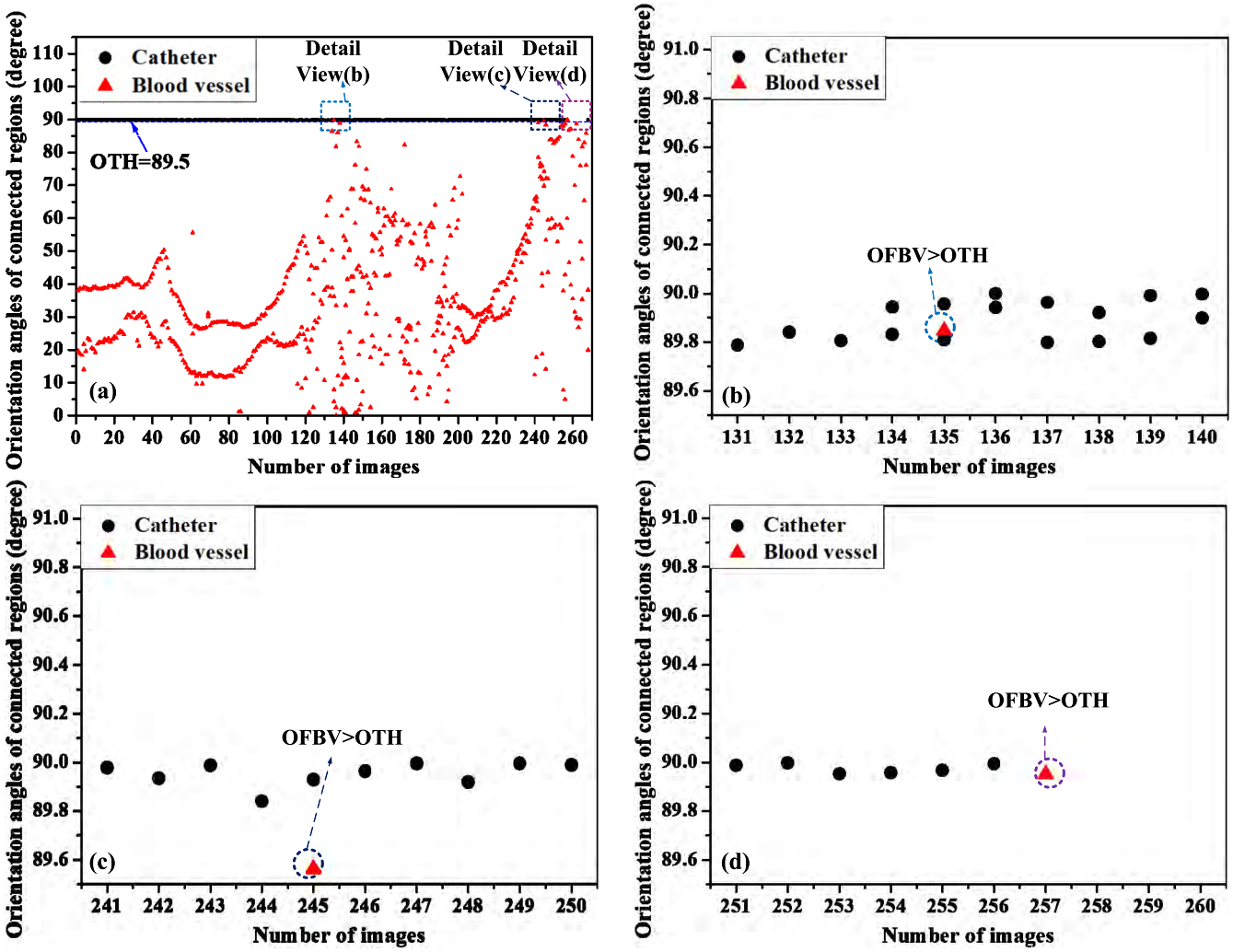

FIGURE 5. (a) Orientation distribution of catheters and blood vessels' connected regions from 268 images. (b), (c) and (d) are detail views of (a)'s dashed box. In (b) (c) and (d)'s dashed circles, orientation angles of connected regions are more than the orientation threshold (89.5°) marked as a dash line in (a). OTH: Orientation threshold. OFBV: Orientation of blood vessel.

Figure 6 shows examples of the orientation and area-size of the connected regions. The orientation and area-size of every connected region in images are calculated. We apply the segment condition in (8) to process them and the experimental results are shown in Fig. 7. From Fig. 7, the residual catheter portions have been removed completely. By simultaneously extracting orientation and area-size of connected regions as morphological features, namely applying the segment condition in (8), catheter are removed and the contours of the blood vessels can be accurately distinguished.

The guide-wires in some images are not removed completely as shown in Fig. 7(g) and (h), since guide-wire and blood vessels are connected that becomes one connected region. The total number of these images containing guide-wire and blood vessels connected is 5 and the rate of in 268 images is 1.8657%, which is very small. This error can be eliminated by an easy method, which is presented in Section II D.

D. CORRECTION OF GUIDE-WIRE CONECTING BLOOD VESSELS

Firstly, we need to discern the images of guide-wire and blood vessels connecting. Comparing with Fig. 7(f) and (g), when the guide-wire is removed completely, a black shadow exists on the blood vessel shown in Fig. 7(f), namely, the intensity of some A-scans (ρ direction) of the image are all zero. Whereas, when the guide-wire is not removed, the guide-wire will at the front of the shadow along the ρ direction and the intensity of all A-scans will not be zero. Based on this phenomenon, the images of guide-wire and blood vessels connecting are identified easily.

Secondly, we locate and remove the guide-wire from the images that contain guide-wire and blood vessels connecting. Here we apply a method by combining of intensity and the length of guide-wire features to locate and remove the guide-wire [13].

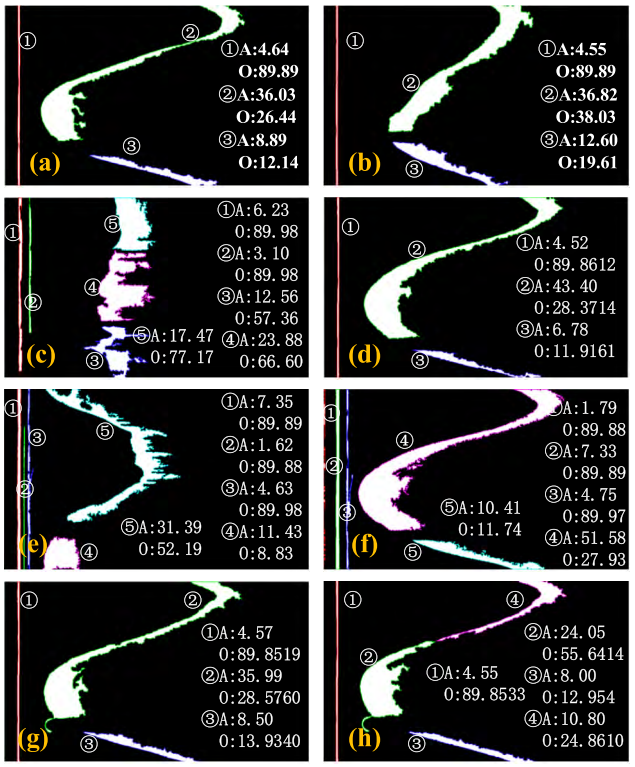

FIGURE 6. Examples of the orientation angle and area-size of the connected region. A: Area-size (unit:*10^{-2}mm^2), O: Orientation angle (uint: degree).

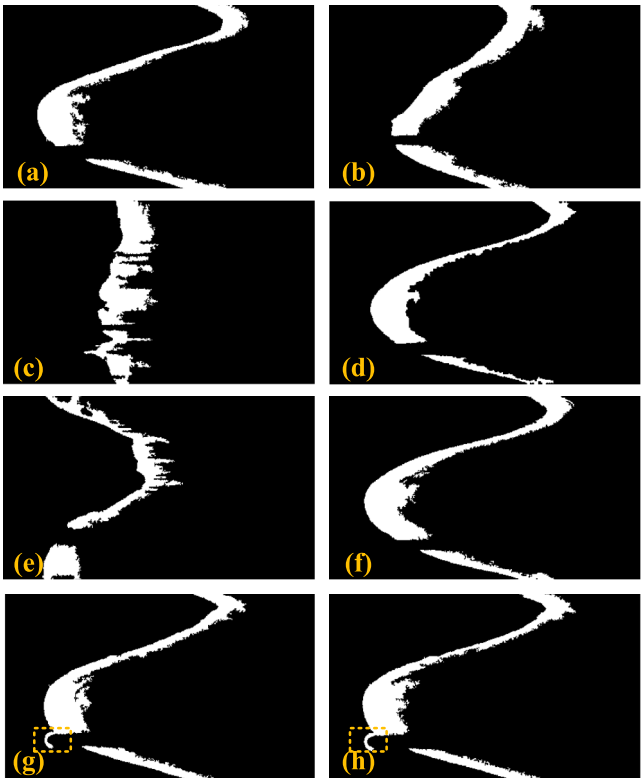

FIGURE 7. Examples of the results using segment condition based on simultaneously extracting orientation and area-size morphological features. The guide-wires in (g) and (h) are not removed.

E. CONTOUR DISCRIMINATION AND RECONSTRUCTION OF INCOMPLETE CONTOUR

We search the location of the first pixel with an intensity of 1 as the lumen contour for each A-scan (ρ direction) in the image shown in Fig. 8 (a) and (b).

Since a black shadow exists on the blood vessels and the discriminated lumen contour (marked as a red line) is not complete shown in Fig. 8(b), we apply a bicubic interpolation compensation method to reconstruct the missing lumen contour caused by the guide-wire's shadow. After that, the missing on the lumen contour is reconstructed shown in Fig. 8(c).

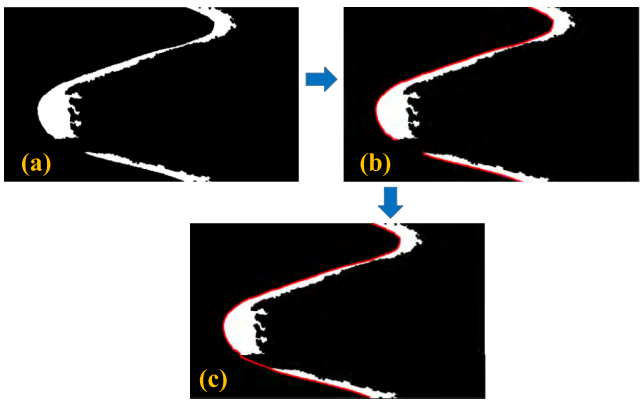

FIGURE 8. (a) Connected regions of blood vessels. (b) Discriminated results of lumen contour with the missing part. (c) Reconstructing results of the missing contour of the lumen by a bicubic interpolation.

F. COORDINATE TRANSFORMATION

The bilinear interpolation of the image in the polar coordinate system is used and then we can get images in Cartesian coordinates. The final discriminated results of lumen contour marked as a red line are shown in Fig. 9.

III. VALIDATION METHODS AND RESULTS

The presented lumen segmentation method is validated through directly comparison to the manual annotations made by one independent expert observer blinded to automated segmentation results (considered as ground truth). A set of five metrics [9], [26]–[28] are used to measure the accuracy of the presented method. These metrics are described below:

(1) Dice coefficient (*DICE*) [19], [29], [30]

$$DICE = \frac{2 \cdot (V_{seg} \cap V_{gt})}{V_{seg} + V_{gt}} \times 100\%, \tag{9}$$

where V_{seg} is the area-size of automatically segmented regions, V_{gt} is the area-size of manually segmented regions. Here the area-size of segmented regions is the right part separated by the vessel contour in images with polar coordinates. $V_{seg} \cap V_{gt}$ is area-size of the overlapping lumen regions of image segmented by automatic method and manual method.

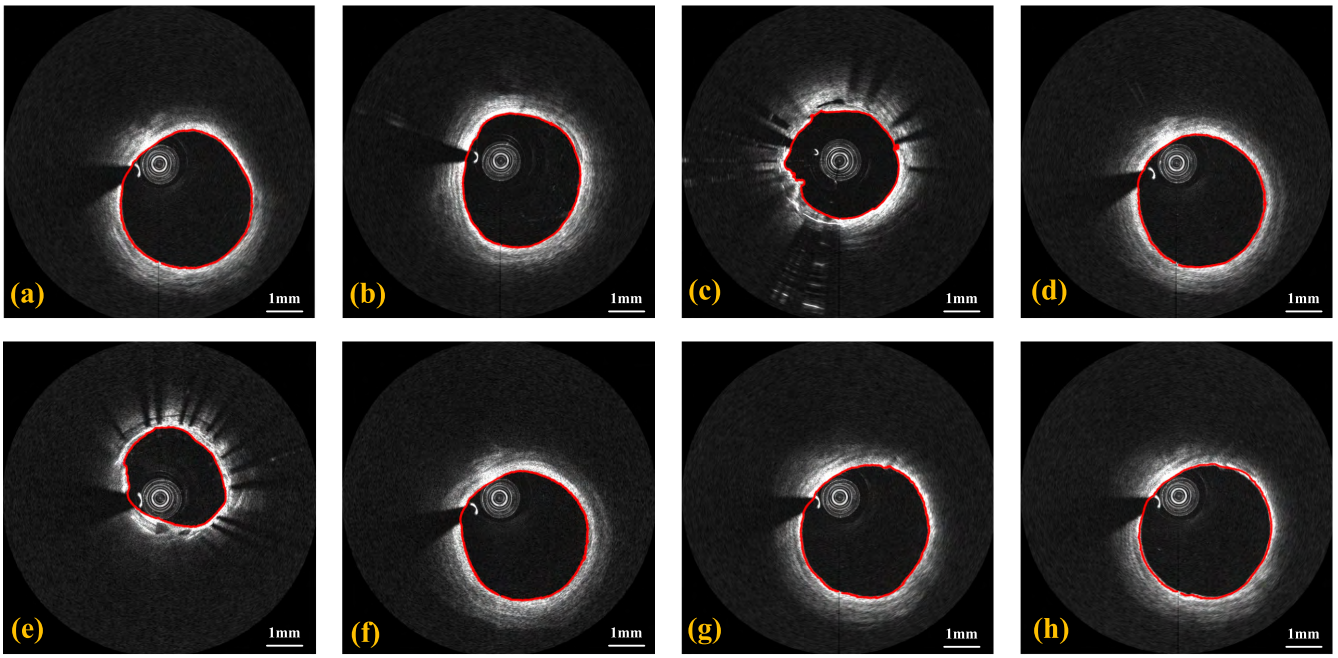

FIGURE 9. Discriminated results of lumen contour marked as a red line on images in Cartesian coordinate.

DICE falls in the interval of [0-100%], it represents the similarity between the two segmentations, therefore, the higher the *DICE*, the more close the automatic segmentation to manual segmentation.

(2) Hausdorff distance (H) [21]

$$H = \max\{\max_{seg\in SEG}\{\min_{gt\in GT}\{dist(seg, gt)\}\}, \times \max_{gt\in GT}\{\min_{seg\in SEG}\{dist(seg, gt)\}\}\}, \quad (10)$$

where *seg* and *gt* are pixels of the lumen contour obtained with the automatic and the manual segmentation respectively. *SEG* and *GT* are the lumen area from automated segmentation and manual segmentation. *dist* represents the distance between the two pixels.

(3) Jaccard index (*JS*) [14]

$$JS = \frac{V_{seg} \cap V_{gt}}{V_{seg} \cup V_{gt}} \times 100\%, \quad (11)$$

The value of *JS* represents the overlapping area ratio between automatic and manual segmentation. The value of *JS* is between 0 and 100% for the worst and the best situation, respectively.

(4) Accuracy (*ACC*) [21], [30]

$$ACC = \frac{TP + TN}{TP + FP + TN + FN} \times 100\%, \quad (12)$$

$$TP = SEG \cap GT, \quad (13)$$

$$FP = SEG - (SEG \cap GT), \quad (14)$$

$$TN = \overline{SEG \cup GT}, \quad (15)$$

$$FN = GT - (SEG \cap GT), \quad (16)$$

where *TP* is true positive, *FP* is the false positive, *TN* is the true negative and *FN* is the false negative. *TP*, *FP*, *TN* and *FN* are obtained from relations based on (13)-(16). The value of *ACC* falls in the interval of [0-100%]. The higher *ACC*, the higher similarity between automated and manual segmentation.

TABLE 2. Results of automated lumen segmentation.

Symbol	Quantity
DICE (%)	99.32±0.58
H (mm)	0.06±0.52
JS （%）	99.40±0.42
ACC （%）	99.66±0.25

We obtain the averaged and the standard deviation of these metrics using automatic segmentation and manual segmentation. The results of these parameters we calculated are shown in the TABLE 2. For the studies [19], [29], [30], the *DICE* matrix achieved values from 97±1.5 (%) to 97.8±2.16 (%), while our proposed method presented the *DICE* of 99.32±0.58, which is comparable to the literature [19]. *H* in our present method is 0.06±0.52mm, which is much lower than the value of the same parameter of 0.17±0.22mm [21]. As for the value of *JS*, the value of our method is 99.40±0.42 (%), which is higher than the *JS* of 95.6% in [14]. As for the value of *ACC* by our presented method is 99.66±0.25 (%), which is comparable to the *ACC* values which are from 99.77±0.25 (%) to 99.8±0.21 (%) in [21].

A linear regression is used to characterize the degree of association between the manual and automated segmentation

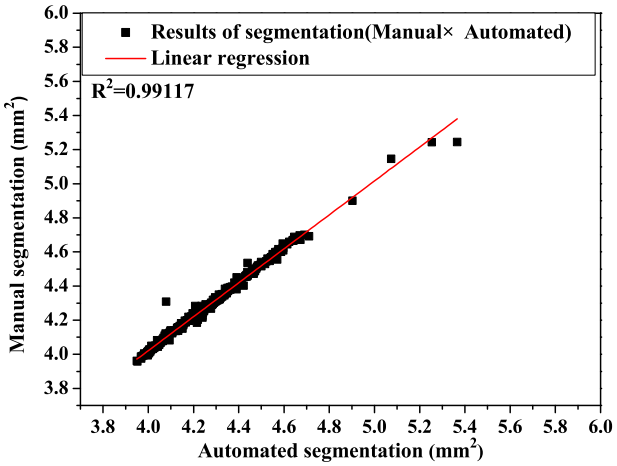

FIGURE 10. The linear regression of manual and automated segmentation for the lumen contour.

results. The values of V_{seg} and V_{gt} are shown in Fig. 10. The consistency of V_{seg} and V_{gt} are reflected by the slope of the fitting line. The slope of the fitting line is 0.99485, nearly equals to 1 shown in Fig. 10. R square in our linear regression equals to 0.99117, which presents a good match of automatic and manual segmentations. Here values of V_{seg} and V_{gt} are related to locations of vessel contours in images, which is unrelated to the degree of association between manual and automated segmentation results.

IV. CONCLUSIONS

We present a simple and effective method for automatic lumen segmentation method in IVOCT based on morphological feature extraction. We use image enhancement, median filtering, image binarization and morphological closing operation to reduce speckle noise, minimize the effect of blood artifacts and fill in small holes inside the vascular wall. We extract the orientation and area-size of connected regions as morphological features in images and remove the catheter and guide-wire completely by morphological corrosion operation, small area-size region removal and orientation morphological feature comparison. And then the contour of the lumen can be discriminated. The evaluation metrics of this method, Dice index, Hausdorff distance, Jaccard index and Accuracy of 99.32%, 0.06 mm, 99.4% and 99.66%, respectively are obtained from comparing with expert annotations on 268 IVOCT images. Compared with other lumen segmentation methods based on morphological operations, the presented method can remove the catheter and guide-wire completely, even if the catheter and guide-wire cling to the lumen or the shape of catheter is irregular. Since only the morphological operations are used to complete all processes, the calculation burden is reduced greatly.

The data set in our experiment is 268 images, which sample number is a relatively small. The reason is that the manual segmentation by an expert is a time-consuming work. In future, we will consider to increase the sample number.

REFERENCES

[1] G. J. Tearney, M. E. Brezinski, S. A. Boppart, B. E. Bouma, N. Weissman, J. F. Southern, E. A. Swanson, and J. G. Fujimoto, "Catheter-based optical imaging of a human coronary artery," *Circulation*, vol. 94, no. 11, p. 3013, Dec. 1996.

[2] J. G. Fujimoto, S. A. Boppart, G. J. Tearney, B. E. Bouma, C. Pitris, and M. E. Brezinski, "High resolution *in vivo* intra-arterial imaging with optical coherence tomography," *Heart*, vol. 82, no. 2, pp. 128–133, Aug. 1999.

[3] I. K. Jang, G. Tearney, and B. Bouma, "Visualization of tissue prolapse between coronary stent struts by optical coherence tomography," *Circulation*, vol. 104, no. 22, p. 2754, Nov. 2001.

[4] B. E. Bouma, M. Villiger, K. Otsuka, and W.-Y. Oh, "Intravascular optical coherence tomography [Invited]," *Biomed. Opt. Express*, vol. 8, no. 5, pp. 2660–2686, May 2017.

[5] A. Giannopoulos, Y. S. Chatzizisis, and G. D. Giannoglou, "Optical coherence tomography: An arrow in our quiver," *Expert Rev. Cardiovascular Therapy*, vol. 10, no. 5, pp. 539–541, Jan. 2014.

[6] H. Zafar, F. Sharif, and M. J. Leahy, "Feasibility of intracoronary frequency domain optical coherence tomography derived fractional flow reserve for the assessment of coronary artery stenosis," *Int. Heart J.*, vol. 55, no. 4, pp. 307–311, Jul. 2014.

[7] A. Karanasos, J. Ligthart, K. Witberg, G. V. Soest, N. Bruining, and E. Regar, "Optical coherence tomography: Potential clinical applications," *Current Cardiovascular Imag. Rep.*, vol. 5, no. 4, pp. 206–220, Aug. 2012.

[8] Z. Wang, D. Chamie, H. G. Bezerra, H. Yamamoto, J. Kanovsky, D. L. Wilson, M. A. Costa, and A. M. Rollins, "Volumetric quantification of fibrous caps using intravascular optical coherence tomography," *Biomed. Opt. Express*, vol. 3, no. 6, pp. 1413–1426, Jun. 2012.

[9] Y. Cao, Q. Jin, Y. Chen, Q. Yin, X. Qin, J. Li, Rui Zhu, and W. Zhao, "Automatic side branch ostium detection and main vascular segmentation in intravascular optical coherence tomography images," *IEEE J. Biomed. Health Inform.*, vol. 22, no. 5, pp. 1531–1539, Sep. 2018.

[10] Z. Wang, H. Kyono, H. G. Bezerra, D. L. Wilson, M. A. Costa, and A. M. Rollins, "Automatic segmentation of intravascular optical coherence tomography images for facilitating quantitative diagnosis of atherosclerosis," *Proc. SPIE*, vol. 7889, Feb. 2011, Art. no. 78890N.

[11] Y. Cao, K. Cheng, X. Qin, Q. Yin, J. Li, R. Zhu, and W. Zhao, "Automatic lumen segmentation in intravascular optical coherence tomography images using level set," *Comput. Math. Methods Med.*, vol. 2017, Feb. 2017, Art. no. 4710305.

[12] S. Joseph, A. Adnan, and D. Adlam, "Automatic segmentation of coronary morphology using transmittance-based lumen intensity-enhanced intravascular optical coherence tomography images and applying a localized level-set-based active contour method," *J. Med. Imag.*, vol. 3, no. 4, Nov. 2016, Art. no. 044001.

[13] J. M. Amrute, L. S. Athanasiou, F. Rikhtegar, M. José, T. G. Camarero, and E. R. Edelman, "Polymeric endovascular strut and lumen detection algorithm for intracoronary optical coherence tomography images," *J. Biomed. Opt.*, vol. 23, no. 3, Mar. 2018, Art. no. 036010.

[14] M. Miyagawa, M. G. F. Costa, M. A. Gutierrez, J. P. G. F. Costa, and C. F. F. C. Filho, "Lumen segmentation in optical coherence tomography images using convolutional neural network," in *Proc. IEEE 40th Annu. Int. Conf. Eng. Med. Biol. Soc. (EMBC)*, Honolulu, HI, USA, Jul. 2018, pp. 600–603.

[15] Y. L. Yong, L. K. Tan, R. A. McLaughlin, K. H. Chee, and Y. M. Liew, "Linear-regression convolutional neural network for fully automated coronary lumen segmentation in intravascular optical coherence tomography," *J. Biomed. Opt.*, vol. 22, no. 12, Dec. 2017, Art. no. 126005.

[16] H. Soltanizadeh and S. R. Oshterinan, "Fully automated lumen detection in intravascular OCT images by using fuzzy system," *Int. J. Eng. Technol.*, vol. 2, no. 4, pp. 388–389, 2014.

[17] H. Modanloujouybari, A. Ayatollahi, and A. Kermani, "Vessel wall detection in the images of intravascular optical coherence tomography based on the graph cut segmentation," in *Proc. Iranian Conf. Elect. Eng. (ICEE)*, Tehran, Iran, May 2017, pp. 39–44.

[18] M. D. Xu, J. Cheng, D. W. K. Wong, J. Liu, A. Taruya, and A. Tanaka, "Graph based lumen segmentation in optical coherence tomography images," in *Proc. 10th Int. Conf. Inf., Commun. Signal Process. (ICICS)*, Singapore, Dec. 2015, pp. 1–5.

[19] M. C. Moraes, D. A. C. Cardenas, and S. S. Furuie, "Automatic lumen segmentation in IVOCT images using binary morphological reconstruction," *BioMed. Eng. Online*, vol. 12, p. 78, Aug. 2013. Accessed: Jun. 27, 2017. doi: 10.1186/1475-925X-12-78.

[20] S. Celi and S. Berti, "*In-vivo* segmentation and quantification of coronary lesions by optical coherence tomography images for a lesion type definition and stenosis grading," *Med. Image Anal.*, vol. 18, no. 7, pp. 1157–1168, Oct. 2014.
[21] M. M. G. Macedo, W. V. N. Guimarães, M. Z. Galon, C. K. Takimura, P. A. Lemos, and M. A. Gutierrez, "A bifurcation identifier for IV-OCT using orthogonal least squares and supervised machine learning," *Comput. Med. Imag. Graph.*, vol. 46, pp. 237–248, Dec. 2015.
[22] W. Hatta, K. Uno, T. Koike, S. Yokosawa, K. Iijima, A. Imatani, and T. Shimosegawa, "Optical coherence tomography for the staging of tumor infiltration in superficial esophageal squamous cell carcinoma," *Gastrointestinal Endoscopy*, vol. 71, no. 6, pp. 899–906, May 2010.
[23] G. J. Ughi, T. Adriaenssens, W. Desmet, and J. D'hooge, "Fully automatic three-dimensional visualization of intravascular optical coherence tomography images: Methods and feasibility *in vivo*," *Biomed. Opt. Express*, vol. 3, no. 12, pp. 3291–3303, Dec. 2012.
[24] F. Chaumette, "Image moments: A general and useful set of features for visual servoing," *IEEE Trans. Robot.*, vol. 20, no. 4, pp. 713–723, Aug. 2004.
[25] Z. Huang and J. Leng, "Analysis of Hu's moment invariants on image scaling and rotation," in *Proc. 2nd Int. Conf. Comput. Eng. Technol.*, Chengdu, China, Apr. 2010, pp. V7-476–V7-480.
[26] J. K. Udupa, V. R. LeBlanc, Y. Zhuge, C. Imielinska, H. Schmidt, L. M. Currie, B. E. Hirsch, and J. Woodburn, "A framework for evaluating image segmentation algorithms," *Comput. Med. Imag. Graph.*, vol. 30, no. 2, pp. 75–87, Mar. 2006.
[27] M. L. Olender, L. S. Athanasiou, J. M. de la Torre Hernández, E. Ben-Assa, F. R. Nezami, and E. R. Edelman, "A mechanical approach for smooth surface fitting to delineate vessel walls in optical coherence tomography images," *IEEE Trans. Med. Imag.*, vol. 38, no. 6, pp. 1384–1397, Jun. 2019.
[28] H. H. Chang, A. H. Zhuang, D. J. Valentino, and W. C. Chu, "Performance measure characterization for evaluating neuroimage segmentation algorithms," *NeuroImage*, vol. 47, no. 1, pp. 122–135, Mar. 2009.
[29] G. J. Ughi, J. Verjans, A. M. Fard, H. Wang, E. Osborn, T. Hara, A. Mauskapf, F. A. Jaffer, and G. J. Tearney, "Dual modality intravascular optical coherence tomography (OCT) and near-infrared fluorescence (NIRF) imaging: A fully automated algorithm for the distance-calibration of NIRF signal intensity for quantitative molecular imaging," *Int. J. Cardiovascular Imag.*, vol. 31, no. 2, pp. 259–268, Feb. 2015.
[30] Z. Wang, H. Kyono, H. G. Bezerra, H. Wang, M. Gargesha, C. Alraies, C. Xu, J. M. Schmitt, D. L. Wilson, M. A. Costa, A. M. Rollins, and A. M. Rollins, "Semiautomatic segmentation and quantification of calcified plaques in intracoronary optical coherence tomography images," *J. Biomed. Opt.*, vol. 15, no. 6, Nov. 2010, Art. no. 061711.

HUISHUO ZHAO was born in Shijiazhuang, Hebei, China. She received the B.S. degree in photoelectric information science and engineering from Hebei University, Hebei, China, in 2017. She is currently pursuing the M.S. degree with the School of Precision Instruments and Opto-electronics Engineering, Tianjin University. Her research interests include optical coherence tomography (OCT) and image processing.

BIN HE was born in Jiangxi, China. He is currently pursuing the B.S. degree with the School of Precision Instruments and Opto-electronics Engineering, Tianjin University, Tianjin, China. He is an Intern with the State Key Laboratory of Low Dimensional Quantum Physics, Department of Physics, Tsinghua University, and the Collaborative Innovation Center of Quantum Matter, Beijing. His current research interests include optical coherence tomography (OCT) and digital picture processing.

ZHENYANG DING received the B.S. degree in opto-electronics information engineering and the M.S. and Ph.D. degrees in optical engineering from Tianjin University, Tianjin, China, in 2008, 2010, and 2013, respectively. From 2013 to 2015, he was a Postdoctoral Researcher with the University of Maryland, College Park, MD, USA. He is currently an Associate Professor with the School of Precision Instruments and Optoelectronics Engineering, Tianjin University. His research interest includes optical coherence tomography.

KUIYUAN TAO received the B.S. degree in opto-electronics engineering from Tianjin University, Tianjin, China, in 2008, and the M.S. degree in optical engineering from Nankai University, Tianjin, in 2011. He is currently pursuing the Ph.D. degree with the School of Precision Instruments and Opto-electronics Engineering, Tianjin University. His current research interest includes optical coherence tomography (OCT).

TIANDUO LAI was born in Zhejiang, China. He received the B.S. degree in optoelectronic information science and engineering from Tianjin University, Tianjin, China, in 2018, where he is currently pursuing the M.S. degree with the School of Precision Instruments and Opto-electronics Engineering. His current research interests include optical coherence tomography (OCT) and image processing.

HAO KUANG received the master's degree in management. He is currently the CEO of Nanjing Forssmann Medical Technology Company, Nanjing, China. His current research interest includes optical coherence tomography (OCT).

RUI LIU was born in Jiangsu, China. He received the Ph.D. degree in medical from Second Military Medical University, Shanghai, China, in 2016. He is currently a Neurologist with the Jinling Hospital, Medical School of Nanjing University. His research interest includes the use of optical coherence tomography in cerebrovascular disease.

XIAOGUO ZHANG was born in Jiangsu, China. He is currently a Technologist-in-Charge with the Heart Intervention Center, Zhongda Hospital, Southeast University, Jiangsu, China. His current research interests include optical coherence tomography (OCT) and intravascular ultrasound (IVUS).

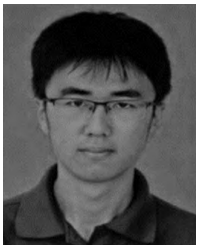

YICHENG ZHENG was born in Shandong, China. He is currently pursuing the B.S. degree with the School of Precision Instruments and Opto-electronics Engineering, Tianjin University, Tianjin, China. His current research interest includes optical coherence tomography (OCT).

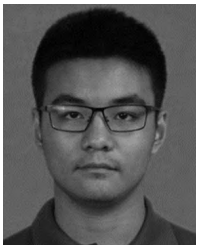

JUNYI ZHENG was born in Tianjin, China. He is currently pursuing the B.S. degree with the School of Precision Instruments and Opto-electronics Engineering, Tianjin University, Tianjin, China. His current research interest includes optical coherence tomography (OCT).

TIEGEN LIU received the B.S., M.S., and Ph.D. degrees from Tianjin University, Tianjin, China, in 1982, 1987, and 1999, respectively, where he is currently a Full Professor with the School of Precision Instrument and Optoelectronics Engineering. His research interests include optical coherence tomography (OCT) and optical fiber sensing.